Experimental studies of the vapor phase nucleation of refractory compounds. V. The condensation of lithium

Frank T. Ferguson
Department of Chemistry, Catholic University of America, Washington, D.C. 20064

Joseph A. Nuth III
Code 691, NASA-Goddard Space Flight Center, Greenbelt, Maryland 20771

(Received 22 February 2000; accepted 13 June 2000)

Lithium nucleation was studied over the range of 830–1100 K in a gas evaporation apparatus yielding supersaturation ratios of approximately 300 to 7 over this temperature range, respectively, at an estimated flux of 10^9 $cm^{-3}s^{-1}$. During runs we observed the same fluorescence phenomena due to atomic lithium vapor and the lithium dimer as noted by other researchers. The measured supersaturations are much higher than the values predicted by Classical Nucleation Theory. Modifications to Classical Nucleation Theory to account for the presence of dimers in the lithium vapor do not seem to account for this discrepancy. The data and Scaled Nucleation Theory agree fairly well at the lower temperature range, but at the higher end of the temperature range the data have a steeper drop in the supersaturation values than predicted by Scaled Nucleation Theory. © *2000 American Institute of Physics.* [S0021-9606(00)01234-4]

I. INTRODUCTION

There has been considerable experimental and theoretical research on the gas phase nucleation of volatile substances such as water, alcohols and a variety of organic compounds. These materials typically nucleate under low supersaturation, low nucleation flux conditions and, despite its obvious shortcomings, the Classical Nucleation Theory (CNT),[1] often does a fair job in predicting the condensation behavior of these compounds. In contrast, experimental nucleation data on metals and other refractory compounds are typically characterized by high degrees of supersaturation and fluxes and little, if any, agreement between data and the Classical Nucleation Theory or its modifications such as that by Lothe and Pound.[2,3]

To date, the only agreement between experimental nucleation data for a refractory species and Classical Nucleation Theory is a study of cesium by Cha *et al.* using an upward thermal diffusion cloud chamber.[4] Rudek *et al.* have recently repeated these cesium experiments using a newly redesigned thermal diffusion cloud chamber and were able to extend the temperature range of the cesium data by operating the chamber in the downward mode.[5,6] In the upward mode, phoretic forces placed a lower temperature limit on the available data range. By operating in the downward mode these forces become negligible and these researchers were able to extend the range of critical supersaturation data for cesium over the temperature range of 289–554 K. In order to achieve reasonable agreement between the Internally Consistent Classical Theory (ICCT) and the data, the ICCT needed to be modified by a factor of 2. It should be noted that this behavior is quite similar to that found in lower-temperature, nonmetallic systems such as *n*-alkanes.[5]

In addition to the diffusion cloud chamber, refractory nucleation has been studied using the shock tube technique[7,8] and the gas evaporation method.[9–11] The cesium diffusion cloud chamber study is the only known agreement between the Classical Theory and refractory nucleation—the only other agreement between experiment and theory is for several gas evaporation studies of silver, SiO and magnesium and Scaled Nucleation Theory (SNT).[11,12] In general the data from these three experiments are consistent with the predictions of Scaled Nucleation Theory, although it should be noted that a more detailed inspection of the magnesium study showed that some of the parameters derived from the data were slightly outside the range predicted by the theory.[11]

The goal of this work is to provide additional data on the condensation of refractory materials and to compare these data with the predictions of both Classical Nucleation Theory (CNT) and Scaled Nucleation Theory (SNT). We have chosen lithium in this study because of its relatively high volatility in comparison with other refractories and because of its predicted similarity to previous work on magnesium. Another interesting feature of lithium is that the equilibrium vapor contains a small quantity of lithium dimer at higher temperatures.

Several researchers have studied the evaporation and condensation of alkali metals in the past. Mann and Broida studied the plasma resonance light scattering of these species using a gas evaporation apparatus over pressure ranges from 0.5 to 200 Torr.[13] Vapor leaving the furnace condensed into particles which the authors estimated to be approximately 5 nm in diameter and these particles tended to grow as they traveled in the flowing inert gas stream. For lithium in particular, Mann and Broida observed fluorescence from the 670.8 nm resonance transition of the lithium atom and between 460–550 nm due to the lithium dimer. Mochizuki and Sasaki recently made a more refined spectral analysis of the thermal evaporation of lithium, measuring the extinction spectra as both a function of heating time and position above the crucible source.[14] Depending upon operating conditions,

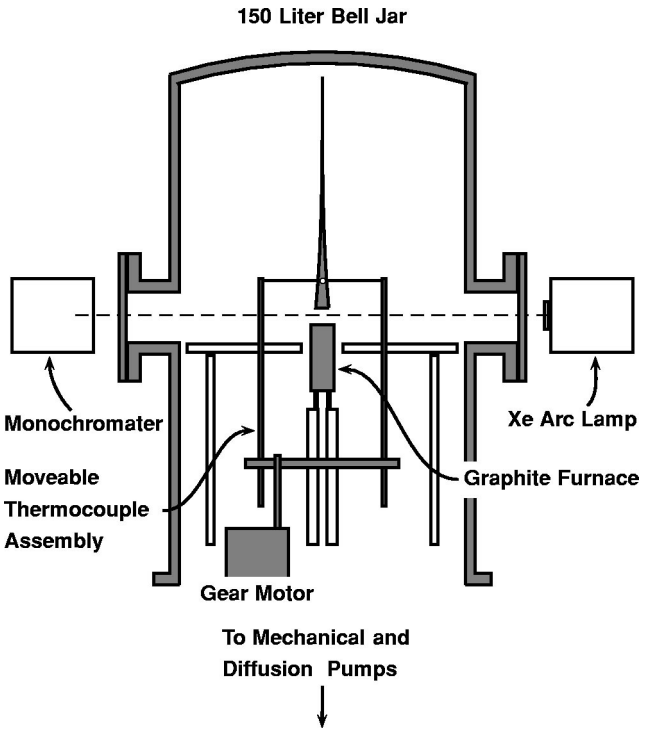

FIG. 1. Cross-sectional diagram of the experimental apparatus.

the authors were able to produce two distinct zones; one consisting mostly of lithium atoms and dimers and a second containing larger aggregates or ''microcrystals.'' Like Mann and Broida, Mochizuki and Sasaki measured a sharp spectral line at 670.8 nm due to the $S-P$ electronic transition of atomic lithium. Later as the temperature of the crucible source increased (thereby increasing the lithium vapor concentration) broad bands appeared at 600–800 nm and at 450–550 nm; both of these features are evidence of the lithium dimer.

II. EXPERIMENT

A cross sectional diagram of the apparatus used in this work is shown in Fig. 1. The gas evaporation apparatus is similar to the one used in previous experiments and the reader is referred to these works for more detailed descriptions.[9–11] The material to be vaporized is placed within a small electrically heated furnace and this furnace assembly is enclosed within a stainless steel bell jar. During an experiment the chamber is evacuated using a combination of mechanical and diffusion pumps and filled with a moderately low (100–300 Torr) pressure of helium. Heating is initiated and, at a sufficiently high temperature, a buoyant plume of condensing refractory material forms approximately 1–2 cm above the crucible. There is a distinct interface between the vapor-rich region just above the crucible and the particle-rich region of the smoke plume.

Temperature at the crucible source is measured using a stainless steel sheathed, 0.32 cm (0.125 in) diameter, type-K thermocouple while the temperature at the smoke cloud interface is measured using a movable thermocouple assembly. This assembly consists of two stainless steel rods attached to a moveable stage which can be used to track the slight movements of the vapor/smoke interface. A thin-wire, 0.0254 cm (0.010 in.) diameter, uninsulated type-K thermocouple is stretched across the two leads such that the junction is placed directly over the center of the crucible. Placing the thermocouple in this manner provides the maximum amount of rigidity in junction location, while maintaining a minimum amount of disturbance to the smoke cloud.

In previous work, the concentration of the generated vapors was not measured directly, but estimated using a simple model of the vapor transport. Because of the strong convective currents in the system it has typically been assumed that the refractory vapor is confined to a buoyant plume and is undiluted from its crucible source. The vapor pressure at this source can be estimated from the measured temperature of the crucible and equilibrium vapor pressure data.

To test this assumption and to provide a more direct method of measuring the vapor concentration we have added a monochromater to the gas evaporation system so that the concentration can be measured directly using a simple atomic absorption measurement. Signal intensity is measured using a photomultiplier detector and the monochromater can be scanned over the desired wavelengths via computer control. A xenon arc lamp provides a continuum light source for the absorption measurement and is also used to illuminate the smoke cloud for viewing. To provide an estimate of the nucleation flux a series of particle extinction measurements were made using the same arc lamp and monochromater system. Unfortunately, because of the lack of available ports and space these extinction measurements could not be performed in conjunction with the nucleation measurements, but were performed under conditions as near to those of the nucleation measurements as possible.

In previous experiments with magnesium, the metal was heated within an alumina crucible surrounded by a tungsten heater basket. This assembly did not work for lithium because of the extremely corrosive nature of the hot liquid lithium. When heated, the liquid lithium would quickly corrode and destroy the alumina crucible. Mann and Broida[13] noted this same corrosive attack by lithium and it is presumably the reason Mochizuki and Sasaki used a stainless steel crucible in their work.[14] Because of this problem the furnace assembly has been changed from the design used in previous experiments to the one shown in Fig. 2. To contain the lithium we fabricated a crucible from a cylindrical rod of stainless steel. A 1.27 cm (0.5 in.) diameter hole was drilled in the top to accommodate the lithium metal while a thermowell was drilled through the bottom for the crucible thermocouple probe. This allowed accurate measurement of the crucible temperature without intimate contact with the corrosive lithium, thereby increasing thermocouple life. The temperature inside the furnace was checked by placing a thermocouple in an empty crucible and running the system over the temperature range of interest. This steel crucible was electrically insulated from the furnace using an alumina tube. For the furnace element we opted to switch to a graphite furnace which provided more uniform heating of the crucible and a greater temperature operating range than the tungsten baskets used previously.

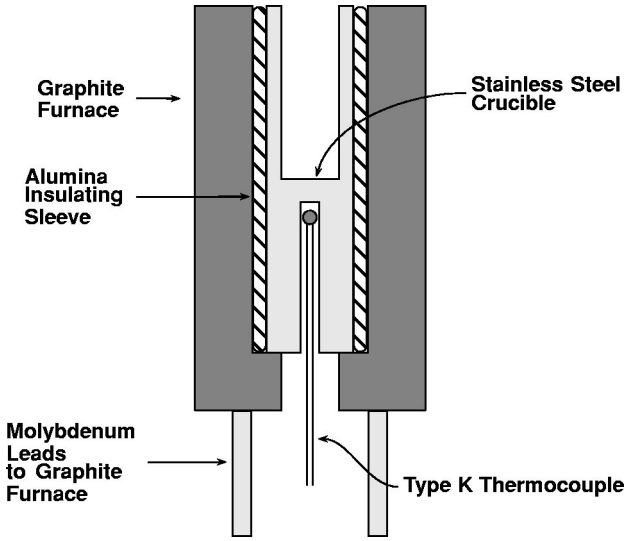

FIG. 2. Cross-sectional diagram of the stainless steel crucible and furnace assembly.

III. RESULTS

A. Calibration and test of the absorption system

To test and calibrate the absorption system we constructed the small cell and furnace assembly shown in Fig. 3. As shown in the figure there is a small, hollow steel calibration cell which has caps on both ends. A small hole is placed in the body of the cell and a thermocouple is inserted into this thermowell to measure the temperature of the cell. The cell is enclosed within a large graphite heater and this heater is covered with a cylindrical piece of steel in order to minimize radiative losses from the heater. Two different size cells are used to provide different absorption path lengths, but both are shorter in length than the graphite heater so that temperature gradients within the cell are minimized. The system is oriented in the bell jar apparatus such that the arc lamp/monochromater optical path falls through the centerline of the cylindrical steel cell.

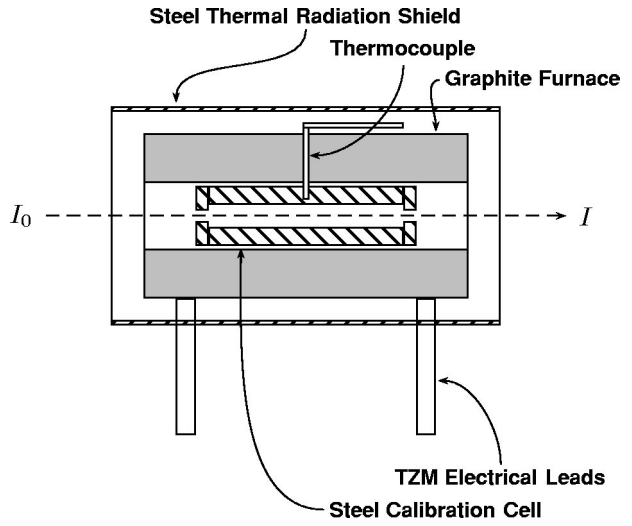

FIG. 3. Steel cell and graphite furnace assembly used to calibrate and test the absorption system.

During a calibration run, lithium metal is placed within the cell and heated to various temperatures at a total helium pressure of approximately 200 Torr. When the temperature of the cell is steady, the absorption spectra of the lithium vapor is measured using the arc lamp and monochromater. The concentration of lithium vapor used in this work is relatively high and the absorption features are significantly broadened by the pressure and doppler terms. Therefore, a curve of growth analysis is used to correlate the vapor concentration with the measured absorption signal.

The equivalent width, W_ν, of a spectral absorption line is given by[15]

$$W_\nu = \int \frac{I_0 - I_\nu}{I_0}\, d\nu = \int 1 - \frac{I_\nu}{I_0}\, d\nu, \tag{1}$$

where I_0 is the intensity of the light source, I_ν is the frequency dependent intensity after absorption, and the integration is taken over the frequency range of the absorption feature. Substituting the Beer–Lambert Law gives

$$W_\nu = \int 1 - \exp[-k_\nu L]\, d\nu. \tag{2}$$

where k_ν is the absorption coefficient and L is the path length over which absorption occurs. The absorption coefficient of a line at a frequency, ν_0, is assumed to follow a Voigt profile, namely,

$$k_\nu = k_0 \frac{a}{\pi} \int_{-\infty}^{+\infty} \frac{\exp[-y^2]}{a^2 + (\omega - y)}\, dy, \tag{3}$$

where k_0 is the absorption coefficient broadened by the Doppler term alone. The term, a, is the natural damping ratio or the Voigt damping ratio of the distribution and is given by

$$a = \left[\frac{\Delta\nu_N + \Delta\nu_L}{\Delta\nu_D}\right]\sqrt{\ln 2} \tag{4}$$

and represents the ratio of the natural, $\Delta\nu_N$, and Lorentzian, $\Delta\nu_L$, broadening terms to the Doppler broadening, $\Delta\nu_D$. In Eq. (3),

$$\omega = \frac{2(\nu - \nu_0)}{\Delta\nu_D}\sqrt{\ln 2} \tag{5}$$

and

$$y = \frac{2\delta}{\Delta\nu_D}\sqrt{\ln 2}, \tag{6}$$

where δ is a variable distance from the point, $(\nu - \nu_0)$.

The term k_0 is the purely Doppler-broadened absorption coefficient and is given by

$$k_0 = \frac{2}{\Delta\nu_D}\sqrt{\frac{\ln 2}{\pi}}\frac{\pi e^2}{m_e c} N f, \tag{7}$$

where N is the number of absorbing species, m_e and e are the mass and charge of an electron, respectively, c is the speed of light, and f is the oscillator strength of the absorption line.

When the absorbing sample is optically-thin, i.e., $(k_\nu L \ll 1)$, the equivalent width is given by

TABLE I. Table of absorption lines and oscillator strengths for the lithium atom.

Wavelength (nm)	Oscillator strength
323.26	0.00552
670.79	0.753

TABLE II. Table of the vapor pressure equation constants used in this work for the lithium atom and dimer.

Species	A	B	C	D
Monomer	10.345 40	8 345.574	−0.000 088 40	−0.681 06
Dimer	18.378 49	11 139.618	0.000 163 42	−3.032 09

$$W_\nu = \frac{\pi e^2}{m_e c} NfL. \tag{8}$$

Therefore a plot of $\log(W_\nu)$ vs $\log(NfL)$ gives a straight line with a slope of 1.0 at these concentrations. It is important to note that if the oscillator strength and path length are accurately known, then there are no other free parameters in the relationship between the equivalent width and concentration in the optically-thin regime. This is not true of samples at higher concentrations. If the sample is optically thick, ($k_\nu L \gg 1$), the equivalent width is

$$W_\nu \propto \sqrt{(NfL)}, \tag{9}$$

so that the slope of the curve changes to 1/2. The point where this transition in slope occurs is governed by the Voigt damping ratio, *a*. Consequently, at these higher concentrations there is an additional unknown which arises in the Lorentzian broadening term,

$$\Delta\nu_L = \frac{2}{\pi}\sigma_L^2 N_2 \sqrt{2\pi RT\left[\frac{1}{M_1}+\frac{1}{M_2}\right]}. \tag{10}$$

In Eq. (10), N_2 and M_2 are the number density and molecular weight of the background gas, respectively, and M_1 is the molecular weight of the absorbing species in the system. The unknown term in Eq. (10) is σ_L^2; it is an effective cross section or optical cross section.

To characterize the system over both the low and high concentration regions, six parameters are needed: the temperature, *T*, the pressure, *P*, the number of absorbers, *N*, the oscillator strength, *f*, the path length, *L*, and the optical collision cross section, σ_L^2. Table I is a list of the two absorption lines for lithium and their oscillator strengths.[16] If the temperature and pressure are known, and *N* is accurately described by the vapor pressure data in this approximately isothermal system, then the only unknown parameter is the optical cross section. Again, it is important to note that this parameter only influences the higher concentration region of the curve of growth.

Throughout this work, vapor pressure data for the lithium atom and dimer were calculated using the following expression:

$$\log(P_v) = A - \frac{B}{T} + CT + D\log(T), \tag{11}$$

where P_v is the vapor pressure in Torr, *A*, *B*, *C*, and *D* are constants in the vapor pressure equation, and *T* is the temperature in Kelvin. The vapor pressure constants for both the monomer and dimer are given in Table II.[17]

Data for the equivalent width for the 670.8 and 323.3 nm absorption lines were taken for two different absorption cell path lengths and the results are plotted in Figs. 4 and 5, respectively. Also shown as insets in these graphs are representative plots of the absorption coefficients from which the curve of growth plots were constructed.

The axes in each plot are scaled by the Doppler width, $\Delta\nu_D$. The 670.8 nm line has a stronger oscillator strength and, at the level of detection of the system, most of the contribution to the equivalent width comes from broadening of the wings of the absorption feature. This region of the curve of growth is dominated by the damping parameter, *a*. The theoretical curve also shown in Fig. 4 is based on an optical cross section, σ_L^2 of 9.8×10^{-16} cm^2. This value was computed based on a best fit to both the 670.8 and 323.3 nm absorption data. For comparison, the gray-shaded area in Fig. 4 shows a 50% variation in this value of the optical cross section. This value for the optical cross section for the lithium–helium system compares favorably with the experimentally measured value of 22×10^{-16} cm^2 for the lithium–nitrogen system given by James and Sugden.[18]

In Fig. 5, the lower concentration region of the 323.3 nm data lies on the theoretical curve. This is encouraging since there are no adjustable parameters in this section of the curve of growth. This lends confidence to the fact that the absorption system, the method of data analysis, and the vapor pressure data used are fairly accurate. Unlike the 670.8 nm data, the 323.3 nm data has a region where much of the increase in the equivalent width comes from an increase in the peak

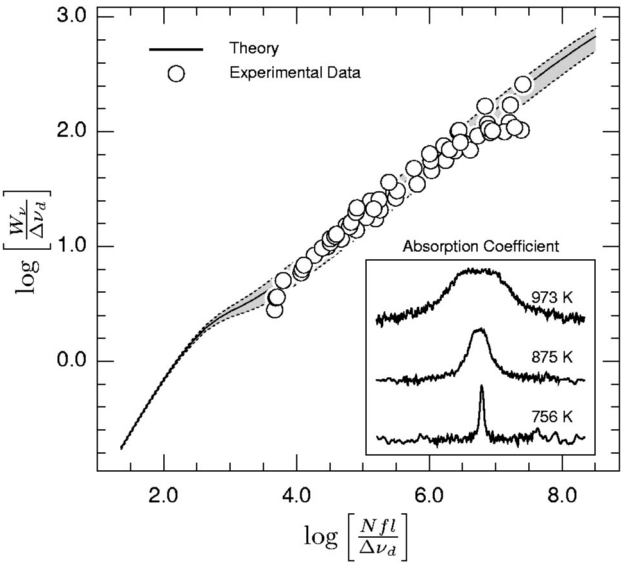

FIG. 4. Curve of growth plot for the 670.8 nm absorption feature from the calibration cell data. The theoretical curve of growth is based on an optical cross section of σ_L^2 of 9.8×10^{-16} cm^2 and the shaded area shows a 50% variation in this cross section and its effect on the theoretical curve of growth.

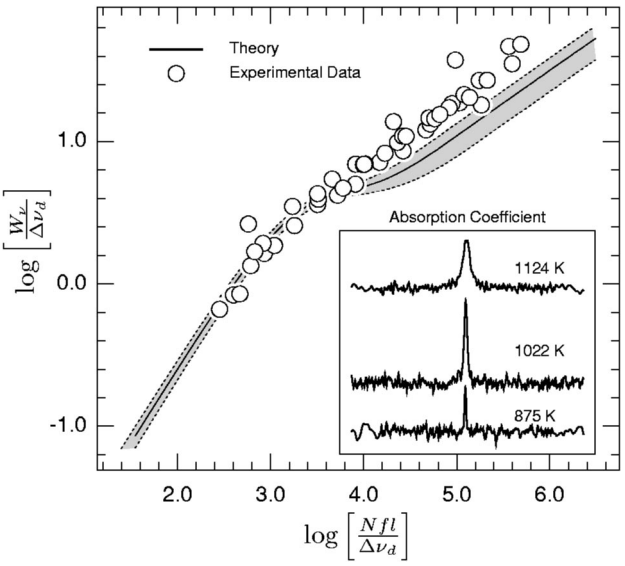

FIG. 5. Curve of growth plot for the 323.3 nm absorption feature from the calibration cell data. The theoretical curve of growth is based on an optical cross section of σ_L^2 of 9.8×10^{-16} cm^2 and the shaded area shows a 50% variation in this cross section and its effect on the theoretical curve of growth.

height. Later, with increasing concentration, most of the contribution to the equivalent width comes from broadening of the line.

In the 323.3 nm data there is some deviation between the data and the theoretical prediction. These data represent the highest temperatures (and hence concentrations) in the cell. There are end caps which enclose the cylindrical steel cell, but vapor can still escape through the tiny holes used for optical access. At the very highest concentrations we believe the amount of escaping vapor effectively increases the path length and therefore leads to higher values for the equivalent width than expected for this region.

B. Lithium evaporation

In our experiments we observed the same lithium vapor fluorescence phenomena as recorded by Mann and Broida[13] and Mochizuki and Sasaki.[14] As the temperature is increased during a typical run, a faint orange–red glow appears by eye extending radially above the crucible; this glow is due to the 670.8 nm transition noted by both Mann and Broida[13] and Mochizuki and Sasaki.[14] As heating continues the glow becomes stronger and spreads farther from the crucible. Later a green glow appears directly above the top of the crucible—at this time the green glow is still surrounded by the red zone. Smoke eventually begins to form directly above the green region and the red glow is barely visible by eye. Examples of this green fluorescence and smoke formation are shown in Fig. 6.

As shown in the figure there is a strong green glow, due to lithium dimers, and a condensed smoke cloud directly above the glow. Both the green glow and smoke plume are of comparable diameter; the condensed smoke cloud consists of a strong white core with blue edges.

Being able to view the lithium dimer in our preliminary experiments gave us some insight into the mechanics of the vapor transport. It is quite likely that the glow of the dimer is a visual indicator of the region of highest concentration. In our previous work with magnesium it was assumed that the vapor leaving the top of the crucible was confined to a buoyant plume and that the magnesium vapor concentration was essentially undiluted from that of the vapor source. Since in the old configuration the crucible opening was very nearly the same diameter as the heater itself, the diameter of the condensing smoke plume was almost always the same size as the crucible diameter due to the upwelling, thermal convective currents along the side of the heater basket. In the new configuration, the cross-sectional area of the crucible opening is roughly 1/16 of the size of the total furnace cross-sectional area and hence there is much more spread in the vapor with increasing temperature and/or decreasing pressure. To test this hypothesis we varied the chamber pressure while maintaining a constant source temperature. We found that with a decreasing pressure there was a conical spread in the lithium dimer glow and a corresponding spread in the diameter of the smoke cloud. In addition the measured condensation temperature also dropped with decreasing pressure. Examples of this spread are shown in Figs. 6(a)–6(c). In each digitized photograph the temperature of the crucible source is approximately the same, but the vapor cloud has spread as the pressure has been dropped from 195 Torr as shown in Fig. 6(a) to 25 Torr as shown in Fig. 6(c). Also as the spread has become greater, the density of smoke particles appears slightly lower than at the higher pressures and the edges of the smoke plume appear bluer in color. These tests

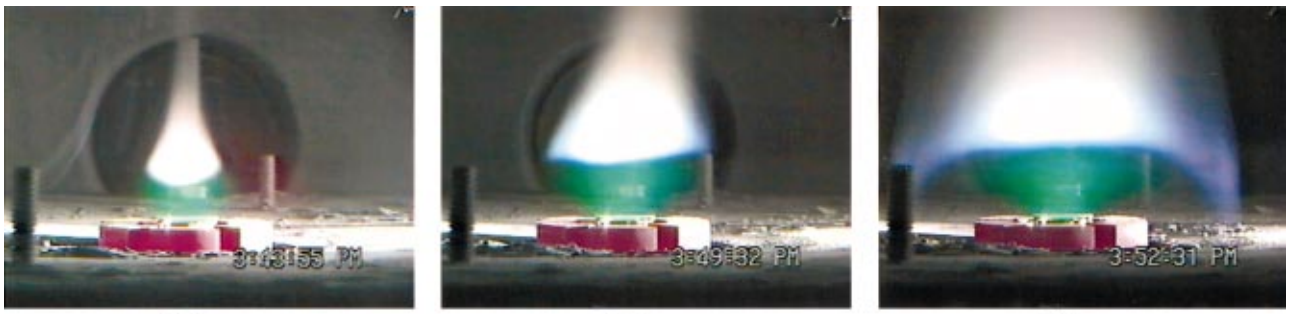

FIG. 6. (Color) Changes in the lithium smoke cloud vapor transport with pressure. The crucible sources shown in each of the photographs are at approximately the same temperature (~1230 K). The chamber pressure in each case is (a) 195 Torr, (b) 50 Torr, and (c) 25 Torr.

suggest a drop in vapor concentration due to dilution. This dilution may be due to enhanced diffusion at lower pressures/higher temperatures or decreased confinement by the convective flows, or a combination of the two. In summary, we decided to apply a simple correction for the spread of the vapor based on the width of the dimer–smoke interface relative to the diameter of the crucible source.

As in the work with magnesium it is assumed that the vapor concentration within the crucible can be given by the equilibrium vapor pressure of the metal at the temperature of the crucible. During a run the resulting smoke cloud is captured on videotape. Later this video is digitized and these digitized data are used to calculate the diameter of the condensation plume. If the plume diameter and crucible opening are of comparable size, then the vapor concentration should be nearly identical to that of the source. Otherwise a correction factor based on the ratio of the cross sectional area of the plume and of the crucible opening is applied to the calculated vapor pressure. In the runs that we have performed this correction ranges down to about 0.06 (for a smoke plume several times larger in area than the crucible opening). Implicit in this assumption is that the vapor spreads out uniformly from the source.

The atomic absorption measurements will provide a test of whether this assumption about the spread of the vapor is justified when the data collected by the two methods is compared. Even before this comparison, there are several indications that this is probably the case. First, as shown in Fig. 6, there is obviously a spread in the lithium vapor. As the vapor spreads, though, both the dimer concentration and the density of the smoke cloud appear to be uniform by eye in the radial direction. Second, the lithium nucleation front usually tends to be flat and probably lies on an isotherm. If the vapor profile were concentrated in a certain region, e.g., along the centerline, nucleation would occur closer to the heater at this point and farther away from the heater at the edges [see Fig. 6(a)]. The only way that the nucleation front would remain fairly flat with an uneven spread in vapor is if the temperature profile was exactly tailored to compensate for the variations in the concentration, a highly unlikely situation.

C. Concentration of the lithium dimer

The green fluorescence of the lithium dimer is quite strong and the question arises whether there is a significant enhancement of the dimer concentration in the plume over that expected from its equilibrium vapor pressure. At the typical temperatures of the experiment, the equilibrium mole fraction of the dimer is roughly 0.5%–3%. Using the calibration cell data and several measurements of the typical plume found in our nucleation experiments, we were able to check for any significant departures from these equilibrium values.

This check was done by measuring the equivalent width of the lithium dimer feature with respect to the equivalent width of the lithium atom absorption feature. By comparing equivalent widths of these features and not converting to absolute concentrations, departures from equilibrium are easily seen without introducing possible errors due to path length measurements.

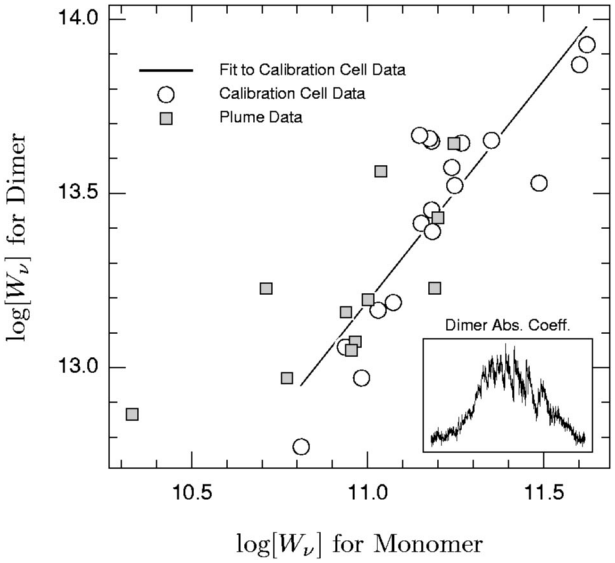

FIG. 7. Comparison of the equivalent widths of the lithium dimer feature and the equivalent width for the monomer at 323.26 nm. Shown in the inset is a typical dimer absorption coefficient spectrum used to prepare the plot.

Spectral scans were made of the monomer and dimer features in the calibration cell and the results are shown in Fig. 7. These cell data are plotted as circles in the figure and are fitted by a least squares line. Also shown as an inset in the figure is a representative plot of the dimer absorption coefficient used to calculate the data. Although there is considerable scatter in this fit, there seems to be a direct, roughly linear relationship between the strength of the dimer feature and the monomer absorption. The unconfined plume data are shown as gray squares in Fig. 7. Most of these data points follow the same trend, while there are a few points above and to the left of the fitted line. From these data it appears that there is no significant enrichment of the dimer in the plume over the data obtained in the equilibrium cell.

D. Extinction measurement

In a previous study with magnesium we did not attempt to measure the nucleation flux, but merely reported our best estimate of this value. To provide a more confident estimate of the flux in this case we performed a simple particle extinction measurement using the same monochromater/arc lamp system as used in the absorption measurements. This is done by moving the heater assembly down slightly so that the optical path passes through the condensed smoke particles.

The attenuation of the light intensity, I, by the smoke particles is given by the Beer–Lambert law,

$$I = I_0 \exp[-\gamma L], \tag{12}$$

where I_0 is the unattenuated intensity, γ is the extinction coefficient, and L is the length over which extinction occurs. For a polydisperse system of spherical particles, the extinction coefficient at any wavelength, λ, is given by

$$\gamma(\lambda) = \sum_i \left(\frac{\pi}{4} d_i^2\right) N(d_i) Q_{\text{ext}}(d_i, \lambda, m), \tag{13}$$

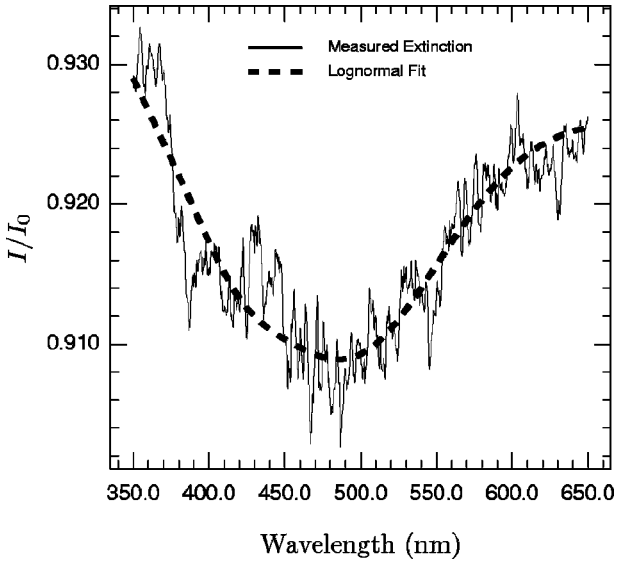

FIG. 8. Plot of the measured particle extinction spectra and of a least-squares lognormal particle size distribution fit to the data. The fitted data yield a geometric mean particle diameter, d_g, of 267 nm and a geometric standard deviation of, σ_g, of 1.13. The total number density of particles is calculated as $\sim 2.0\times 10^7$ cm^{-3}.

where d_i is the diameter of particles of size i, $N(d_i)$ is the total number of particles of size, i, and Q_{ext} is the extinction efficiency factor of particles of size, i, at wavelength, λ, and complex index of refraction, m. In Eq. (13), the summation is over all particles sizes.

Assuming a lognormal distribution of particle sizes (typical of gas condensed particles), the function $N(d_i)$ can be described by three parameters: N_{total}, the total number of particles in the system and the two parameters characterizing the size distribution, the geometric mean diameter, d_g, and the geometric standard deviation, σ_g.

In this work, the extinction was measured over the wavelength range of 350–650 nm. This measurement was made while the plume was extremely steady and typical of the kind observed during the nucleation runs. The pathlength over which extinction occurred was measured from digitized video images of the plume during the run and the extinction efficiency factor was calculated using Mie scattering theory for the various particle sizes, wavelengths and refractive indexes. Data for the wavelength dependent refractive indexes were taken from Ref. 19.

With these data available, the only unknowns in the system are the total number of particles and the two parameters characterizing the lognormal distribution, d_g and σ_g. Figure 8 is a plot of the measured extinction spectra of the lithium smoke plume. At each of these points, there will be an extinction that depends on these three unknowns: N_{total}, d_g, and σ_g. A least squares fit to the data points making up Fig. 8 yields a geometric mean diameter, d_g, of 267 nm, a geometric standard deviation, σ_g of 1.13, and a total concentration of particles of N_{total} of $\sim 2.0\times 10^7$ cm^{-3}. This fitted result is also shown by the larger, dashed line in Fig. 8. For a lognormal distribtuion, 67% of the particles lie within the size ranges of (d_g/σ_g) and $(d_g\sigma_g)$. In this particular case, these limits correspond to 235 and 303 nm, respectively. Particles produced by gas condensation tend to have a fairly narrow size distribution and these data seem to indicate that this is the case for these lithium particles. These particle sizes and the size-distribution data are also similar to measurements made in our lab by two different methods (photon correlation spectroscopy and SEM analysis) on magnesium using a similar gas-evaporation apparatus.[20] It is also important to note that at the point where the extinction is measured, the particles have probably undergone most of their growth. The initially condensed particles are expected to be much smaller.

To calculate the flux of particles we must still estimate the velocity of the particles in the plume at the point of measurement. Based on numerical simulations of the flow we estimate a plume velocity of ~ 30 to 50 cm s^{-1}, and this implies a nucleation flux of $\sim 10^9$ cm^{-3} s^{-1}.

E. Nucleation data

As stated earlier, a xenon arc lamp was used to illuminate the lithium smoke front. Because of the low ionization potential of lithium (5.4 eV), it is possible that the arc lamp could cause ion-induced nucleation. To test for this possibility we made a series of runs in which the position of the smoke cloud was compared using the arc lamp and a He–Ne laser beam (632.8 nm). If ion-induced nucleation is significant, the position of the nucleation front should change with the switch from the arc lamp to laser illumination. We did not observe any discrepancy in the position or shape of the nucleation front and conclude that ion-induced nucleation is not a significant effect in this work.

Data were collected over an ambient pressure range from 100 to nearly 300 Torr. At lower pressures the spread in the smoke cloud was more pronounced and at higher temperatures the flow within the chamber became less stable and more ''turbulent.'' An ambient pressure of approximately 200 Torr provided a good compromise between these two effects and most of the data were collected at this pressure.

As noted earlier, nucleation data were collected by two methods: the temperature at the point of nucleation was measured and (1) the vapor-phase lithium monomer concentration was estimated by a spectroscopic measurement of the vapor concentration, or (2) the vapor-phase lithium monomer concentration was estimated by measuring the temperatures of the crucible source and assuming uniform expansion for the vapor transport. In both cases the width of the condensing plume was measured. For the spectroscopically-determined data, this width was used as the path length over which absorption occurred. For the temperature/model-determined data it was used to determine the dilution factor applied to the vapor concentration. As explained earlier, this dilution factor was taken as the ratio of the area of the vapor source (area of the crucible opening) to the cross-sectional area at the point of condensation (cross-sectional area of the base of the condensing plume).

The spectroscopic data are plotted in Fig. 9. These data cover a 270 K temperature span and the supersaturations range from ~ 200 at 830 K to ~ 10 at 1100 K. Unfortunately, there is a large amount of scatter in the data and fewer points at the highest temperatures.

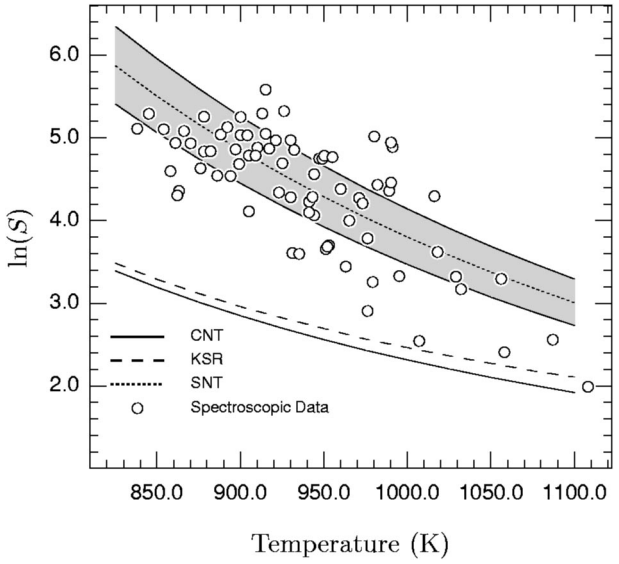

FIG. 9. Nucleation data collected from the absorption spectra of the 323 nm line. Also shown in the plot are the predictions of Classical Nucleation Theory (CNT), Katz–Saltsburg–Reiss Theory (KSR) for associated vapors, and Scaled Nucleation Theory (SNT). The gray shaded area are the predictions of Scaled Nucleation Theory based on a lithium critical temperature of 2700 ± 100 K.

For comparison, the predictions of Classical Nucleation Theory are also plotted in this figure. Classical Nucleation Theory predicts the following relationship for the condensation flux, J:

$$J = \left(\frac{2\sigma}{\pi m}\right)^{1/2} V N_1^2 \exp\left[\frac{-16\pi\sigma^3 V^2}{3k^3T^3(\ln S)^2}\right], \tag{14}$$

where σ is the surface free energy, m is the mass of the condensing molecule, V is the volume of the condensing molecule, N_1 is the number density of the monomer, and k is Boltzmann's constant. The Classical Nucleation Theory curve shown in Fig. 9 is found by solving Eq. (14) for S over the temperature range using the bulk density of lithium, the lithium surface free energy of 398 erg cm^{-2} (Ref. 21) (value of the surface free energy at the melting point), and our estimate of the flux ($\sim 10^9$ cm^{-3} s^{-1}) calculated in the previous section. All of the spectroscopically determined data points lie above the CNT predictions.

Because the flux in Eq. (14) is so sensitive to the value of the surface free energy, the large discrepancies between the CNT and the data can be resolved by using a larger value of the surface tension. For example, using the melting point value of the surface tension, 398 erg cm^{-2}, CNT would predict fluxes as high as 10^{20}–10^{22} cm^{-3} s^{-1} for the supersaturation values measured in this work. Yet these fluxes are reduced to $\sim 10^9$ cm^{-3} s^{-1} if the value of the surface tension is increased to approximately ~ 550 erg cm^{-2}—a roughly 40% increase over the melting point value.

There is an interesting contrast between this work with lithium and previous work with magnesium. A comparison between the magnesium data and classical theory showed that, using a value of the bulk surface tension for magnesium at the melting point, classical theory greatly underpredicted the possible range of fluxes. Also since much of the magnesium condensation temperature data fell below the melting point and presumably the solid magnesium would have a higher surface energy than that of the liquid, the fluxes calculated via classical theory could be even smaller. In the case of lithium, all of the data has been collected above the melting point and therefore the surface tension should be lower than the melting point value used in this analysis. Yet, a lower value of the surface tension would predict even higher fluxes, thus increasing the discrepancy between the data and classical theory.

Lithium has a small, but appreciable concentration of dimer in its equilibrium vapor. Katz, Saltsburg, and Reiss (KSR), developed a modification to CNT to account for the presence of such associated species.[22] Counter to intuition, higher critical supersaturations are needed when associated species are present over the case where only the monomer is present. Alternatively, this means that, for a given supersaturation, the flux of particles is reduced in the presence of associated species. For some vapors in which only $\sim 1\%$–2% of the vapor is associated, the effect can be so small as to be masked by the uncertainty in the experiment. Katz *et al.* does give an example for bismuth in which the results are more dramatic. Bismuth at 1100 K is nearly an equimolar mixture of the monomer and dimer. Classical Nucleation Theory would predict a critical supersaturation of 13.9 at this temperature. In contrast, after accounting for the associated species, this value is increased to 46.0—a dramatic change in the critical supersaturation.[22]

Talanquer and Oxtoby have recently re-examined gas–liquid nucleation in associating liquids using a density-functional approach to such systems.[23] They note that CNT tends to fail rather drastically in associating systems, yielding critical supersaturations that are often significantly lower than the experimental data. For example Heist *et al.* studied the nucleation of acetic acid which has a very significant concentration of dimer in the vapor.[24] Much of their measured critical supersaturation data were nearly twice as high as the predictions of typical CNT (assuming all monomer in the vapor), and their results were more closely aligned with the KSR predictions. Later experiments with formic and propanoic acids gave similar behavior—experimentally measured critical supersaturations much higher than the typical CNT predictions and just slightly lower than the KSR predicitions.[25] Talanquer and Oxtoby note that CNT tends to underestimate the nucleation barrier height and that KSR corrects much of this error. Talanquer and Oxtoby's density functional approach to the problem predicts critical supersaturations slightly lower than KSR, yet well above the CNT estimate.[23]

To check whether this result would have any significance in this work we recalculated the Classical Theory predictions using the modifications as suggested by Katz *et al.* for associated species. For the concentration of dimers as given by the vapor pressure expressions in Table II, the CNT result and its modifications due to associated species were virtually indistinguishable. Because these vapor pressure data can vary, we also calculated the results based on the dimer data given by Douglas *et al.*[26] The dimer pressures given in this reference are roughly a factor of 2 higher than

those given by the vapor pressure equation in Table II.

Using these new dimer vapor pressure data, a plot of CNT modified to account for association is shown in Fig. 9. Although these data produce an effect on the supersaturation which is noticeable, the change in supersaturation with respect to typical CNT values is many times smaller than the experimental error in this work. In this case the predicted change over the CNT is slight, and the differences between the two predictions increase very slightly towards higher temperatures where the relative amount of dimer in the vapor increases.

Scaled Nucleation Theory predicts the following relationship between the critical supersaturation, S_{cr} and the condensation temperature, T for a flux of 1 $cm^{-3}s^{-1}$,[27]

$$\ln S_{cr} \approx \Gamma \Omega^{3/2} \left[\frac{T_c}{T} - 1 \right]^{3/2}. \tag{15}$$

The quantity Ω denotes the negative partial derivative with respect to temperature of the surface tension per molecule (also known as the excess surface entropy per molecule) and typically ranges from 1.5 to 2.2—for most substances Ω has a value of approximately 2.0. T_c is the critical temperature of the material, and Γ is a weak function of the temperature and supersaturation, approximately equal to 0.53. For fluxes larger than 1 $cm^{-3}s^{-1}$, the critical supersaturation is modified as follows:

$$\ln S \approx \ln S_{cr} \left[1 + \frac{\ln J}{(2 \ln J_{cr})} \right] = \ln S_{cr} \cdot Q, \tag{16}$$

where the term $\ln(J_{cr})$ is approximately equal to 72 ± 3 and Q represents the bracketed term. For materials in which the critical temperature is not known, Eq. (15) can be rearranged to

$$(\ln S)^{2/3} = (\Gamma Q)^{2/3} \Omega \left[\frac{T_c}{T} - 1 \right] \tag{17}$$

such that a plot of $\ln(S)^{2/3}$ vs $(1/T)$ should produce a straight line.

Although the critical temperature is unknown, it can be estimated as $T_c \sim (T_b/0.6)$ where T_b is the boiling temperature of the material. The predictions of Scaled Nucleation Theory for lithium, assuming a $T_c \sim 2700$ K and a flux of 10^9 $cm^{-3}s^{-1}$ are also shown in Fig. 9. In this plot, the shaded gray region represents a ± 100 K range in the estimated critical temperature.

Scaled Nucleation Theory predicts higher supersaturation values over this temperature range than does Classical Nucleation Theory and these higher values tend to correspond better with the measured data. At the lower temperatures, this agreement is fairly good, but the data tends to have a steeper drop in supersaturation with temperature than predicted by Scaled Nucleation Theory. It is assumed that the fluxes in this work are fairly constant, very nearly 10^9 $cm^{-3}s^{-1}$. It is very unlikely that a change in the flux could cause such a steep drop in the supersaturation values. For example, consider the data at 1100 K. The supersaturation for SNT was calculated for a flux of 10^9 $cm^{-3}s^{-1}$ and gives a value for $\ln(S)$ of 3.0. Even if the flux was dropped to 1 $cm^{-3}s^{-1}$, SNT would predict $\ln(S)$ of 2.6—still higher than the experimental data at this temperature.

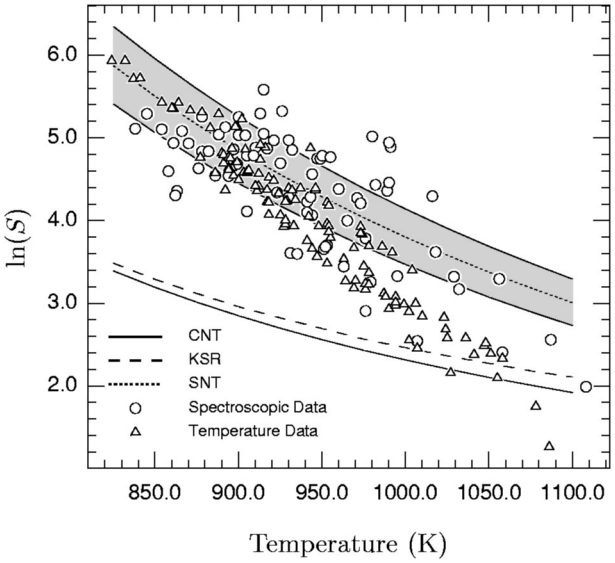

FIG. 10. Comparison of spectroscopically obtained nucleation data and data collected from temperature measurements and assumption about the vapor transport. Also shown in the plot are the predictions of Classical Nucleation Theory (CNT), Katz–Saltsburg–Reiss Theory (KSR) for associated vapors, and Scaled Nucleation Theory (SNT). The gray shaded area are the predictions of Scaled Nucleation Theory based on a lithium critical temperature of 2700 ± 100 K.

The data collected by simply measuring the temperatures and assuming a uniform spread in the vapor are shown in Fig. 10 as the small triangles. For comparison, the same plotting scale is used as in Fig. 9 and predictions of CNT and SNT are also shown in the plot. There tends to be better agreement between the two data collection methods at the lower end of the temperature scale (we note that at these low temperatures, the dimer concentration is quite low). This is encouraging since the spectroscopic data provide a method of checking the accuracy of the results and the previous data collected using this apparatus and method. The temperature-collected nucleation data tend to have a slightly steeper temperature drop than those collected spectroscopically. The supersaturations for these data range from ~ 380 at 830 K to ~ 5 at 1090 K. The scatter in the temperature-collected nucleation data is still high, though not as great as for the spectroscopically collected data. Finally, these data also tend to produce supersaturations more closely aligned with the predictions of SNT than CNT. Taking both sets of data together, we find the supersaturations range from ~ 300 at 830 K to ~ 7 at 1100 K.

In Figs. 9 and 10, the predictions of SNT are plotted by estimating a value for the critical temperature and assuming $\Omega \sim 2.0$ and $\Gamma \sim 0.53$. In previous work we have used our experimental data to calculate these quantities as well as such quantities as the critical cluster sizes over the temperature range studied. These calculations have been done for our experimental data and the results are shown in Table III. The quantities are given for the spectroscopic and temperature-collected data separately as well as for these two data sets

TABLE III. Experimental data sets and predictions of the Scaled Nucleation Theory.

Data set	Slope	Intercept	r^2	T_c (K)	Ω	n_{cr}
Spectroscopic data	4470	−2.15	0.68	2080	2.20	11–32
Temperature data	6390	−4.29	0.91	1490	4.40	1–11
Both sets	5690	−3.52	0.81	1620	3.61	8–21

combined. The derived slope, intercept, squared correlation coefficient, critical temperature, excess surface entropy per molecule and range of critical cluster sizes according to SNT are all shown in the table. The spectroscopic data predict the most reasonable values for the critical temperature, T_c, Ω, and the critical cluster sizes, n_{cr} even though the scatter in this data set is very large. The results for the temperature data alone predict unreasonably low critical temperatures and critical cluster sizes and a high value for Ω.

IV. CONCLUSIONS

Lithium nucleation was studied over the temperature range from 830 to 1100 K in a gas evaporation apparatus yielding supersaturation ratios ~ 300 to ~ 7 over this temperature range, respectively, with an estimated flux of 10^9 $cm^3 s^{-1}$. Upon heating the lithium we observed a faint orange fluorescence, presumably due to atomic lithium vapor. At higher temperatures this orange fluorescence was overshadowed by the strong green fluorescence of the lithium dimer. Changes in the dimer-smoke plume diameter with decreasing pressure/increasing temperature suggested that the vapor concentration was being diluted slightly due to enhanced diffusion/decreased convection or a combination of the two. Therefore we applied a simple correction to account for the apparent spread in vapor with increasing temperature and/or decreasing pressure. These data were also checked via atomic absorption to measure the concentration of the lithium vapor just before the point of condensation. In general the two approaches yield similar results, although there is considerable scatter in the spectroscopically-determined data. At the lower temperature range of the data, where dimers are least important, the agreement between the two approaches is rather good; at the higher temperature ranges the drop in supersaturation with increasing temperature is greater for the temperature-collected data than for the spectroscopic data.

The supersaturation ratios measured in both data sets are larger than those predicted by Classical Nucleation Theory. Modifications to Classical Theory to account for the presence of the dimer in the lithium vapor do not appear to be large enough to account for such a discrepancy. Scaled Nucleation Theory predicts higher supersaturation ratios over this temperature range and the data and this theory tend to be more closely matched. Unfortunately Scaled Nucleation Theory also fails to offer a perfect fit to the experimental data.

[1] R. Becker and W. Döring, Ann. Phys. (Leipzig) **24**, 719 (1935).
[2] J. Lothe and G. M. Pound, J. Chem. Phys. **36**, 2080 (1962).
[3] J. A. Nuth III and F. T. Ferguson, in *Nucleation and Crystallization in Liquids and Glasses*, edited by M. C. Weinberg (American Ceramic Society, Westerville, OH, 1993), Vol. 30, p. 23.
[4] Gyu-Suk Cha, Hermann Uchtmann, Jeffrey A. Fisk, and Joseph L. Katz, J. Chem. Phys. **101**, 459 (1994).
[5] Markus M. Rudek, Jeffrey A. Fisk, Joseph L. Katz, Dirk Beiersdorf, and Hermann Uchtmann, in *Nucleation and Atmospheric Aerosols*, edited by M. Kulmala and P. E. Wagner (Pergamon, Oxford, UK, 1996), p. 65.
[6] Markus M. Rudek, Joseph L. Katz, and Hermann Uchtmann, J. Chem. Phys. **110**, 11505 (1999).
[7] J. R. Stephens and S. H. Bauer, in *Proceedings of the 13th International Symposium on Shock Tubes and Waves* (State University of New York, Albany, New York, 1982).
[8] D. J. Frurip and S. H. Bauer, J. Phys. Chem. **81**, 1001 (1977).
[9] J. A. Nuth, K. A. Donnelly, B. Donn, and L. U. Lilleleht, J. Chem. Phys. **85**, 1116 (1986).
[10] J. A. Nuth and B. Donn, J. Chem. Phys. **77**, 2639 (1982).
[11] F. T. Ferguson, J. A. Nuth III, and L. U. Lilleleht, J. Chem. Phys. **104**, 3205 (1996).
[12] B. Hale, P. Kemper, and J. A. Nuth III, J. Chem. Phys. **91**, 4314 (1989).
[13] D. M. Mann and H. P. Broida, J. Appl. Phys. **44**, 11 (1973); **44**, 4950 (1973).
[14] Shosuke Mochizuki and Mie Sasaki, in *Proceedings of the Science and Technology of Atomically Engineered Materials* (World Scientific, New Jersey, 1996), p. 441.
[15] *Flame Spectroscopy* (Wiley, New York, 1965).
[16] *CRC Practical Handbook of Spectroscopy* (CRC Press, Boca Raton, 1991).
[17] Nesmayanov, *Vapor Pressure of the Elements* (Academic, New York, 1963).
[18] C. G. James and T. M. Sugden, Nature (London) **171**, 428 (1953).
[19] *CRC Handbook of Chemistry and Physics*, 78th ed. (CRC Press, New York, 1997).
[20] B. P. Michael, Ph.D. dissertation, University of Virginia, 1998.
[21] *Metals Handbook*, Desk Edition (American Society for Metals, Metals Park, 1985).
[22] J. L. Katz, H. Saltsburg, and H. Reiss, J. Colloid Interface Sci. **21**, 560 (1966).
[23] V. Talanquer and D. W. Oxtoby, J. Chem. Phys. **112**, 851 (2000).
[24] R. H. Heist, K. M. Colling, and C. S. DuPuis, J. Chem. Phys. **65**, 5147 (1976).
[25] Y. G. Russell and R. H. Heist, J. Chem. Phys. **69**, 3723 (1978).
[26] T. B. Douglas, J. L. Dever, and W. H. Holland, J. Am. Chem. Soc. **77**, 2144 (1955), and reported in Ref. 17.
[27] B. Hale, Phys. Rev. A **33**, 4156 (1986).